The Boronated Scintillator Detector of the ISS-CREAM Experiment

Y. Amare[a], T. Anderson[b], D. Angelaszek[a,c], N. Anthony[c], K. Cheryian[c], G.H. Choi[d], M. Copley[a], S. Coutu[b,*], L. Derome[f], L. Eraud[f], L. Hagenau[c], J.H. Han[a], H.G. Huh[a], Y.S. Hwang[g], H.J. Hyun[g], S. Im[b], H.B. Jeon[g], J.A. Jeon[d], S. Jeong[d], S.C. Kang[g], H.J. Kim[g], K.C. Kim[a], M.H. Kim[a], H.Y. Lee[d], J. Lee[d], M.H. Lee[a], J. Liang[c], J.T. Link[g,j], L. Lu[c], L. Lutz[a], A. Menchaca-Rocha[e], T. Mernik[a], J.W. Mitchell[g], S.I. Mognet[b], S. Morton[c], M. Nester[c], S. Nutter[i], O. Ofoha[a], H. Park[g], I.H. Park[d], J.M. Park[g], N. Picot-Clémente[a], R. Quinn[c], E.S. Seo[a,c], J.R. Smith[a], P. Walpole[a], R.P. Weinmann[a], J.Wu[a], Y.S. Yoon[a]

[a]*Inst. for Phys. Sci. and Tech., University of Maryland, College Park, MD 20742, USA*
[b]*Dept. of Physics, Penn State University, University Park, PA 16802, USA*
[c]*Dept. of Physics, University of Maryland, College Park, MD 20742, USA*
[d]*Dept. of Physics, Sungkyunkwan University, Suwon 440-746, Republic of Korea*
[e]*Instituto de Fisica, Universidad Nacional Autonoma de Mexico, Circuito de la Investigación s/n, Ciudad Universitaria, CP 04510 México Distrito Federal, Mexico*
[f]*Laboratoire de Physique Subatomique et de Cosmologie, UJF CNRS/IN2P3 INP, 53 rue des Martyrs, 38026 Grenoble Cedex, France*
[g]*Dept. of Physics, Kyungpook National University, Daegu 702-701, Republic of Korea*
[h]*Astroparticle Physics Laboratory, NASA Goddard Space Flight Center, Greenbelt, MD 20771, USA*
[i]*Dept. of Physics, Geology, and Engineering Technology, Northern Kentucky University, Highland Heights, KY 41076 USA*
[j]*Center for Research and Exploration in Space Science and Technology (CRESST) UMBC, Baltimore MD, 21250*

Abstract

The Cosmic Ray Energetics And Mass for the International Space Station (ISS-CREAM) instrument is a next-generation experiment for the direct detection and study of cosmic-ray nuclei and electrons. With a long exposure in low Earth orbit, the experiment will determine the particle fluxes and spectral details of cosmic-ray nuclei from hydrogen to iron, over an energy range of about 10^{12} eV to $>10^{15}$ eV, and of cosmic-ray electrons over an energy range of about 5×10^{10} eV to $>10^{13}$ eV. The instrument was deployed to the ISS in August 2017 on the SpaceX CRS-12 mission. We review the design, implementation and performance of one of the ISS-CREAM detector systems: a boron loaded scintillation detector used in discriminating electron-induced events from the much more abundant cosmic-ray nuclei.

1. Introduction

The ISS-CREAM instrument is a detector suite designed for flight on the International Space Station (ISS) to measure the composition and energy spectra of cosmic-ray nuclei from 10^{12} eV to $>10^{15}$ eV [1]. Recent measurements [2-4] of elemental spectra of cosmic rays from hydrogen to iron nuclei, at energies up to $\approx10^{14}$ eV, have highlighted the need to refine our understanding of cosmic-ray production and acceleration, presumably in Galactic supernova remnants (for a classic treatment, see [5], for recent modeling work see, e.g., [6-8]). The measured elemental cosmic-ray spectra follow a single power-law distribution in the range 10-100 GeV/nucleon, with a discrepant hardening of the spectra observed

* Corresponding author: sxc56@psu.edu

beginning around 200 GeV/nucleon [2]. A detailed understanding of this effect is needed to improve modeling of the production and transport of Galactic cosmic rays (see, e.g., [8-10]). With a multi-year exposure in low Earth orbit, ISS-CREAM will permit a definitive measurement of the spectral details for individual cosmic-ray nuclei, pushing into the astrophysically interesting "knee" region (at a few times 10^{15} eV). In addition, the small and tantalizing differences in the spectral slopes of hydrogen (2.61 ± 0.01) and helium nuclei (2.55 ± 0.01) [11] need to be refined and measured accurately. The elemental nuclear spectra of all elements need to be measured precisely up to 10^{15} eV and beyond to provide a firm experimental anchor (see, e.g., [12]) on models of cosmic-ray mass composition used in interpreting the results of ground-based studies with air-shower arrays, at energies up to 10^{20} eV and beyond. Finally, the relative proportion of secondary nuclei (such as boron, produced by spallation reactions in the interstellar medium) to primary nuclei (such as carbon, originating primarily in the direct cosmic accelerators) will provide much needed clues (see, e.g., [13]) on the details of interstellar propagation of cosmic rays.

In addition to the measurement of cosmic-ray nuclei, ISS-CREAM is sensitive to incident cosmic-ray electrons at energies 5×10^{10} eV to $>10^{13}$ eV, where the upper end is simply limited by the flux of these particles. The discrimination of electrons from the much more abundant protons is accomplished through the study of the shape of the particle shower in the calorimeter, coupled with the reduced harvest of thermal neutrons in an electromagnetic shower. ISS-CREAM is a next-generation instrument along with the AMS-02 [14] (ISS since 2011), NUCLEON [15] (satellite since 2014), CALET [16] (ISS since 2015) and DAMPE [17] (satellite since 2016) missions. The capabilities of the ISS-CREAM instrument are complementary to those of these other projects, as it is optimized for the study of the highest-energy cosmic-ray nuclei practically directly observable. For example, CALET is optimized for the study of cosmic-ray electrons up to $\approx10^{13}$ eV, so that the electron detection capabilities of ISS-CREAM will provide a confirmation and cross-check of CALET measurements.

The ISS-CREAM experiment is comprised of four detector systems with a common readout electronics scheme which provides data acquisition, command and control, power, and housekeeping, as shown in Fig. 1. Two of the detector systems, namely the silicon charge detector (SCD) and the calorimeter (CAL), are adapted from the CREAM balloon instrument [18]. The SCD is a four-layer silicon pin diode array to measure particle charge, with 2688 pixels per layer [19-20]. The CAL measures particle energy utilizing two densified graphite target blocks and a 20-layer scintillating fiber-tungsten calorimeter, for a total of 21 radiation lengths [21]. The other two detector systems on ISS-CREAM were built specifically to enable the instrument to identify and measure cosmic-ray electrons as a secondary science goal. The boronated scintillator detector (BSD), which is discussed further below, measures the late scintillation light and neutron content of showers produced in the CAL. The top and bottom counting detectors (TCD and BCD, respectively) are pixelated photodiode detectors that measure the shape of the particle shower at two locations (before and after the CAL) along the cascade development [22].
The design and operational details of the overall ISS-CREAM instrument are to be found elsewhere [1], but suffice it to say here that there are two primary instrument triggers for event data (including readout of the BSD). The primary high-energy trigger requires at least six consecutive layers of the CAL to each have at least one optical fiber ribbon with a minimum energy deposit, typically about 35 MeV but adjustable to control trigger rates. A secondary trigger requires at least one hit above an adjustable threshold in the TCD and at least two physical regions (defined by the ASIC chips used in TBCD readout) above an independently adjustable threshold of the BCD. The net result is an overall instrument energy threshold of 1 TeV for T/BCD triggers (particularly sensitive to low mass primary cosmic rays such as protons and helium nuclei) and 10 TeV for CAL triggers (particularly sensitive to the more massive nuclei).

The combination of BSD and T/BCD signals allows for the identification of cosmic-ray electrons in addition to the far more abundant nuclei. As the discrimination techniques employed by the TCD and BCD systems are complementary to those of the BSD we will use data from the two detector systems together in addition to signals from the CAL to obtain a high discrimination power between electrons and nuclei (protons in particular). Such high discrimination power is needed in view of the fact that cosmic-ray protons are about 100 times more abundant than electrons at an energy of 10 GeV, 500 times more abundant at 100 GeV, and 1000 times more abundant at 1 TeV.

2. Measurement Technique

The ISS-CREAM BSD is located below the calorimeter and thus is impacted by large numbers of shower particles when a high-energy cosmic-ray nucleus or electron interacts somewhere in the instrument, typically in the graphite target blocks. The BSD aims to enhance the calorimeter's electron identification capability by measuring the late-time (≈several μs) scintillation light and neutron activity produced by cosmic-ray induced showers. In so doing, the BSD derives its electron/hadron discrimination power from the fact that, for showers which produce similar amounts of total energy deposit in the ISS-CREAM CAL, those which are hadronically induced generate roughly an order of magnitude more late scintillation light and neutrons than those originating from electrons. The larger amount of shower particle leakage out of the CAL and into the BSD is a feature of the different shower profiles (hadronic compared to electromagnetic) subjected to the requirement of a similar amount of CAL energy deposit. Meanwhile the thermalized neutron yield is naturally larger for hadronic than electromagnetic interactions.

The primary detector medium of the BSD is a 60 cm × 60 cm × 3.8 cm slab of polyvinyltoluene-based EJ-254 boron-loaded plastic scintillator [21], custom-developed by Eljen Technology[*]. The BSD's scintillator is loaded with 5% elemental boron by weight. Naturally occurring boron has a 20% isotopic abundance of ^{10}B, leading to an overall ^{10}B loading of 1% in EJ-254. Thermal neutrons entering the BSD may undergo the capture process $^{10}B + n \rightarrow {}^{7}Li + \alpha + \gamma$ with capture probability following a decaying exponential of time constant $\tau = (N \sigma v)^{-1}$ where N is the number density of ^{10}B, σ is the cross section for capture, and v is neutron velocity. Below 200 keV, the neutron capture cross section scales as v^{-1} [24], leading to an energy-independent time constant of 2.7 μs for a 1% ^{10}B loading. Literature values for the scintillation yield resulting from a single neutron capture suggest that the light production signal is equivalent to that produced by a 76 keV electron [24], leading to a predicted 570 photons/capture for EJ-254's stated 7500 photons/MeV light yield [23]. The 2.7 μs time constant for neutron capture gives rise to the need to integrate the signal over a period of a few μs. Diminishing returns occur for longer integration times due to the nature of exponential decays.

Design Considerations

In any space mission, minimal mass, physical dimensions, and power consumption are important. Thermal considerations lead to minimum and maximum survival temperatures (−40 °C to +60 °C for the active detector components and −40 °C to +70 °C for the electronics) and operational temperatures (−20 °C to +40 °C for both). A combination of active and passive cooling systems and heaters in the ISS-CREAM instrument maintains these limits. In cases where different materials are mechanically joined

[*] In fact the production of the BSD slab required no fewer than 22 test castings of large, non-boronated slabs to ensure adequate quality controls in producing this unusual material [25].

(e.g., scintillator-to-glass faces of photomultiplier tubes, or PMTs) careful attention is paid to coefficients of thermal expansion and, if needed, a pliable material is used to make the joint (Nusil CV4-2500 RTV).

Electronics components and design choices are predicated on minimizing various potential failures attributable to the effects of ionizing radiation, such as single-event latchups due to through-going charged particles. Potting or conformal coating is used to protect against short-circuiting and the formation of "tin (and other metals) whiskers" [26], a phenomenon whereby lead-less tin (and other) alloys operated in vacuum over long periods develop protruding tendrils which can create short-circuits, increased noise pickup, and (for components subjected to high voltage) an increased probability of corona arcing. Total ionizing dose (TID) is not a concern for the ISS-CREAM payload, since a 2 mm-thick aluminum shield surrounds the instrument support structure, thus reducing the TID experienced by ISS-CREAM components to an acceptable level (less than 1000 rad[Si]/year [27]). Further details of the electronics design are available in chapters 6 and 7 of [28].

The primary cosmic-ray science goals and space available in the ISS-CREAM design restrict the location of the BSD detector to below the calorimeter. Showers are produced (primarily inside the carbon target blocks) in the forward direction, so they pass through the BSD, given the relative thinness of the CAL [21]. The multiple interactions associated with the shower development result in a harvest of fast neutrons being produced (over a broad spectrum up to tens of MeV). Thermalization of some of these neutrons happens rather quickly (μs) in materials with high light-element content, such as hydrogen, which plastic scintillator provides. In addition to the neutron-capture signal in the boronated scintillator material, any slow-to-develop light extending into the several μs range from the main shower event, such as fluorescence in the scintillator, will also contribute to the total light signal captured in the BSD.

Photosensitive devices must be able to recover from the large amount of prompt light generated by the shower particles in the scintillator and still detect the low light levels associated with the delayed fluorescence and neutron capture signals. GEANT4 [29] simulations suggest that showers generated by ≈150 GeV electrons (the lower end of the target range for ISS-CREAM electron detection) yield only a few neutron captures (Poisson distribution with mean of 3.25±0.02). This low rate of events combined with the need to integrate over an extended period of time requires the ability to distinguish single photoelectrons in a low-noise environment. The BSD is designed to look at scintillation light produced 0.9–4.9 μs after the high-energy cosmic-ray particle interacts in the calorimeter. The post-shower minimum safe delayed start time of 400 ns allows most of the BSD PMTs (16 out of 18) to turn on and stabilize after a through-going particle shower, as described in Section 3.1 below. Using a self-coincidence trigger (several kHz) from two permanently activated BSD trigger PMTs (each mounted at the center of opposite faces of the scintillator slab) rather than from the rest of the ISS-CREAM instrument (several Hz) ensures consistent timing in starting the BSD charge integration after a shower has occurred in the calorimeter.

As showers from hadrons and electrons have different profiles and contain different harvests of energetic particles and photons, the scintillation light from neutron captures occurring later than the primary shower signal in principle enables us to discriminate between hadrons and electrons. However the neutron capture signal is small and is in addition to any delayed scintillation light from the prompt shower event. In the range of several μs there is a common assumption of little-to-no residual scintillation light in fast organic scintillators (the EJ-254's fast component is designed to have a rise time of 0.85 ns and a decay time of 1.51 ns [23]), but any residual such amount, even suppressed at the level of 10^{-4} of the incident light intensity, can potentially overwhelm the small neutron-capture light signature. We discovered through electron and pion beam tests at CERN that the BSD can indeed

discriminate between hadrons and electrons [30], however there was significantly more late signal in the scintillator than we expected based on simulations with late light production due solely to neutron captures. Based on the work of [31], we interpret the late light to be dominated by secondary fluorescence in the scintillator. We have presented a model characterizing this effect more fully in [32]. In this paper we focus on the instrumentation of the BSD and present results showing its sensitivity to neutrons and atmospheric muons from laboratory tests.

3. The Boronated Scintillator Detector

3.1 Design

The BSD comprises two custom 6061-T6 black anodized aluminum enclosures: one for the detector (0.063" lid thickness), and another for electronics. The detector enclosure contains the boronated scintillator slab, trigger and so-called "quartet" PMTs. The electronics enclosure contains all of the detector readout, control, housekeeping and communications electronics. Fig. 2 shows the BSD flight hardware mounted on the ISS-CREAM instrument pallet, and Fig. 3 shows a system block diagram of the BSD electronics and detector enclosures and their contents. The BSD hardware has a total mass of 38 kg (33.5 kg for the detector enclosure, 4.5 kg for the electronics enclosure) and draws a total power of approximately 17.6W under full load.

The BSD detector enclosure is a two-piece box as illustrated in Fig. 4, with the lid and box body sealed with an O-ring (sitting in a groove) to prevent light from entering the enclosure. In the center of the enclosure is the 60 cm × 60 cm × 3.8 cm piece of Eljen EJ-254 [23] polyvinyltoluene plastic scintillator loaded with 5% boron. The scintillator is wrapped on top and bottom and two sides with three layers of 0.003"-thick Teflon tape (TaegaTech 4" wide white, standard density) to help reflect back any light that would otherwise escape the detector. The scintillator is sandwiched at the top and bottom and on the two Teflon-wrapped sides with sheets of Poron foam, which provide a shock-absorbing mount to protect the scintillator during transport and launch. The other two sides of the scintillator have only about 15% Teflon coverage, leaving rectangular openings (3.8 cm high by 6.2 cm wide) to allow light detection by Hamamatsu R1924A one inch diameter photomultiplier tubes [33] (with heritage from the SuperTIGER balloon experiment [34] and the RHESSI satellite instrument [35]). This PMT has an anode pulse rise time of 1.5 ns, an electron transit time of 17 ns with a spread of 0.9 ns. Aluminum brackets with a Poron foam cushion are located at the edges and center of these two sides to hold the scintillator in place against any sliding longitudinally within the box. All of the Poron foam surrounding the scintillator is slightly compressed, preloading it, thus holding the scintillator in position.

The BSD utilizes two PMT designs. Two trigger PMTs (one on each side of the scintillator) are used to form a trigger and initiate the BSD electronic readout. Sixteen additional PMTs, arranged in four quartet units, are used to collect the late light present in the BSD scintillator.

- The two trigger-PMT assemblies are located at the center of each of the partially-wrapped sides of the scintillator. Each assembly consists of one R1924A PMT with its own individual power supply connected to a tapered resistor divider chain based on the SuperTIGER base design [34] in a minimal aluminum structural enclosure. Each trigger assembly is mounted to the bottom of the detector enclosure with a ≈1/8 inch air gap between the PMT front face and the scintillator edge. The small gap prevents any mechanical damage to the PMT during small vibrational movements of the scintillator during rocket launch. The trigger PMTs are used to form a timing trigger (a signal at the level of a single minimum-ionizing particle in either of the trigger PMTs)

when the shower of particles from the calorimeter passes through the scintillator. This trigger is used to initiate a rapid high-voltage switching in the quartet PMTs and to define the event zero-time for the charge-integrating electronics.

- A quartet assembly consists of four PMTs and collects late light present in the scintillator from 0.9 to 4.9 μs following the prompt shower event. Each of the four quartet assemblies has its own individual high-voltage supply to power four gain-matched R1924A PMTs. Two quartet assemblies are located along each partially-wrapped edge of the scintillator on either side of the trigger PMT, for a total of 16 quartet PMTs. The aluminum chassis around each assembly is hard-mounted via screws to a clear acrylic optical piece, epoxied using Stycast 1266 to the partially-wrapped edge of the scintillator. The front faces of the quartet PMTs in each assembly interface optically to the acrylic with the Nusil RTV mentioned above. Thus the quartet PMTs move along with any small vibrational motions of the scintillator.

Active PMTs exposed directly to the large light pulses due to the initial charged-particle shower were shown to often saturate in laboratory tests. This in turn led to significant afterpulses caused by signal saturation, indicating the need for a special PMT dynode design to eliminate these afterpulses. The quartet board dynode gating circuitry applies a −12 V reverse bias to dynodes 1 and 2 of the PMTs until a command to switch ON is issued by the BSD electronics. The dynodes then come to their nominal high voltage within 400 ns, but integration start is delayed until 900 ns, beyond which the total integrated signal is found stable within 2.7% over a large dynamic range. This technique is employed in laser-stimulated fluorescence measurements [36] and works very well in the BSD to enable the quartet PMTs to detect the low levels of light present after the initial particle shower. Details of this implementation are found in [37]. Note that by applying a steady voltage to the “dynode ON” (DON) input of the dynode-gating board, PMTs can alternately be made continually sensitive to transient light signals, and so can behave identically to PMTs whose dynode high-voltage bias is provided via a standard resistive divider. To test and calibrate the BSD PMTs, two red LEDs (Kingbright WP424SRDT, peak emission wavelength of 655 nm) are installed at opposite corners of the scintillator, shining into it. These LEDs enable testing the operation of all PMTs as well as providing a coarse gain calibration (e.g., the PMT response to LED flashes at the same intensity is tracked over time and drifts by no more than 7% over 350 days of operation in space).

The BSD electronics enclosure contains the digitization and readout, PMT control, universal serial bus (USB) communication, power conditioning, and triggering and housekeeping electronics that run the BSD detector. This functionality is distributed on five boards which are stacked on ½” standoffs inside the enclosure box.

- Three of these boards have a common design and are known as the front-end electronics (FEE) boards. Each FEE board digitizes signals from six PMTs utilizing a 16-bit ADC (AD7663, 250 kSPS sampling rate). Each channel has two different gain branches (at a relative factor of about 30) which can resolve signals as small as one photoelectron from the R1924A PMT on the high-gain branch, while the low-gain branch allows for the measurement of a maximum charge of $\approx 8\times10^{7}$ pC, corresponding to 5×10^{8} photoelectrons for the tubes at nominal gain (8×10^{6}, at 1200V operation). The FEE boards also have discrimination circuitry enabling the formation of an event trigger, which in turn initiates powering up the first two dynodes of the quartet PMTs and the data-digitization sequence.
- The functionality of the BSD as well as communication with the ISS-CREAM payload [1] are handled by the control board. Communication with the ISS-CREAM science flight computer (SFC) is handled via USB with two independent FX2LP microcontrollers on the control board providing

a redundant communication pathway. The control board also houses an A3P1000 field-programmable gate array (FPGA) which manages all communication and control of the BSD detector system, including event processing and packaging, controlling the PMT high-voltage supply levels, as well as the dynode switching on the quartet PMTs, and also setting discrimination levels for triggers and scalars. The FPGA also facilitates adjustment of the timing of the DON signal as well as when the charge integration window begins and its duration via commands on the ground and in flight.

- The power and housekeeping board receives power from the ISS-CREAM common electronics and conditions it to the voltage levels required by the BSD electronics and PMT assemblies. The board also has circuitry to condition and package voltage, current, and temperature housekeeping information to distribute to the ISS-CREAM common electronics, and a pulser circuit which drives the two LEDs inside the detector.

Fig. 5 shows the timing diagram of the BSD electronics system. A high-energy cosmic ray interacting in the calorimeter will create a shower of charged particles that generates a coincidence trigger from the two trigger tubes viewing the boronated scintillator. Using a coincidence trigger from the BSD rather than from the instrument ensures consistent timing in starting the BSD charge integration after a shower has occurred in the calorimeter. This coincidence trigger quickly initiates a logic signal which causes the first two dynodes of the quartet PMTs to be switched on. This switching causes a transient signal on all the PMTs from turning on the high voltage. A minimum wait of 400 ns is required to ensure that the transient signal has passed and that the high voltage on the PMTs has stabilized before beginning to integrate charge over a window of several microseconds. In flight, the integration window used covers the range of 0.9 to 4.9 μs after the trigger PMT signals. The charge is then digitized and packaged into an event packet which is collected by the ISS-CREAM SFC over the USB interface, if an instrument master trigger has been formed.

3.2 Expected Detector Efficiency and Performance

In a cosmic-ray induced event within the BSD, the number of photons that reach the R1924A PMTs can be calculated using

$$N_{PMT} = N_{pe} \cdot f_{tir} \cdot e^{-d/a} \cdot R_s^b \cdot f_{ed} \cdot f_{geo} = C_{eff} \cdot N_{pe}$$

where N_{PMT} is the number of photons incident on the PMT, N_{pe} is the number of photons created in the scintillator, f_{tir} is the fraction of light that experiences total internal reflection to the edges of the radiator, $e^{-d/a}$ represents the loss due to attenuation where d is the average pathlength the photons travel and a is their attenuation length, R_s is the reflection coefficient of the scintillator surface and b is the average number of times a photon will reflect off this surface, f_{ed} is the number of photons that escape out of the edge, as opposed to getting trapped in the scintillator, and f_{geo} is the fraction of light that is actually incident on the tube. We define the collection efficiency C_{eff} as the ratio between the number of photons incident on a single PMT to the total number of photons produced in the detector. We conservatively estimate the collection efficiency for the BSD to be 0.28%. After folding in the PMT photocathode quantum efficiency of ≈25% at the peak emission of the EJ-254, and assuming that no light is lost in the transition from scintillator to the PMT face, we expect that for every 10,000 photons produced in the detector, about 7 photoelectrons will result in each PMT.

Laboratory measurements were conducted to check the assumptions that went into the above calculation. The minimum ionization energy deposit dE/dx for scintillator is ≈2 MeV/(g/cm^2). With a 3.8 cm-thick scintillator of density 1.026 g/cm^3, a vertically incident cosmic-ray minimum-ionizing particle

(e.g., an air-shower muon) deposits 7.8 MeV of energy as it traverses the scintillator. EJ-254 has a quoted scintillator efficiency of 7500 photons per 1 MeV electron. As muons and electrons are both leptons we would expect that they behave similarly in scintillator, thus we expect a single through-going muon to produce 58,500 photons in the scintillator. Based on the calculation above, we would thus expect to see about 41 photoelectrons in every PMT.

4. Laboratory Testing of Boronated Scintillator Performance

The performance of the BSD was verified experimentally with atmospheric muons, a ^{252}Cf fast neutron source, and electron and pion beams at CERN. Such measurements provide an end-to-end measurement of the performance of the scintillator, PMT sensors and readout electronics.

4.1 Atmospheric Muon Test

The boronated scintillator slab was equipped with PMTs with prototype bases from the development of the final quartet and trigger PMT designs, which utilized the same switching circuitry as the final flight unit but drew high voltage from external supplies. Each PMT base accommodated one PMT which was then optically coupled to the scintillator sides with a compliant silicon cookie, mechanically squeezed between the PMT front face and the scintillator. A pair of external scintillator paddles placed at the center of the BSD was used to form a coincidence trigger on vertical muons passing through the detector. The mean number of photoelectrons measured for centrally located PMTs in the enclosure, in response to a vertically incident muon, was 79 [28]. This is about twice that expected from the rough calculation of Section 3.2, but, given the conservative estimates in the calculation and uncertainties in the laboratory experiment, these are in reasonable agreement.

4.2 ^{252}Cf Test

As discussed in Section 2, the scintillation yield resulting from a single neutron capture is predicted to yield 570 photons/capture for EJ-254. A laboratory test was conducted to verify the sensitivity of the boronated scintillator to thermal neutrons by taking two pieces of scintillator, one unloaded (Eljen EJ-200) and one loaded with boron (Eljen EJ-254) and exposing them to a ^{252}Cf source, a spontaneous fission source of fast neutrons with a mean energy of 2.3 MeV and most probable energy of 1 MeV. Both the boronated and the non-boronated scintillator blocks were expected to see a significant signal rate due to scattering of the source's fast neutron and gamma-ray products. The boron-loaded piece should also have had an additional rate component due to the capture of thermalizing neutrons (stacks of polyethylene sheets were used near the scintillators to thermalize a fraction of the neutrons).

The test setup for this experiment is shown in Fig. 6. Two identically sized pieces of EJ-200 and EJ-254 scintillators, each measuring 5.8 cm × 6.9 cm × 3.8 cm, were stacked on top of each other such that each had the same exposure to the source. Two PMTs were optically coupled to detect light from each block. In between the source and scintillator a lead sheet was placed to attenuate gamma rays from the ^{252}Cf. Polyethelene boards were placed in front and behind the scintillator blocks to help increase the thermal neutron signal over the fast neutron and gamma-ray background.

The high voltage to the PMTs was adjusted to gain-match them based on their atmospheric muon signal and to produce a single photoelectron (pe) signal with amplitude of ≈6mV (known to 10% accuracy). The PMT signals were amplified and then discriminated with a threshold of ≈1/4 pe and the rates were recorded with either a 0.5” or a 1.5” thick piece of lead shielding. The results of these measurements are

shown in Fig. 7, where the integral signal rates above a given threshold voltage are given as a function of this threshold. The horizontal axis values can be converted to pe units using a 1 pe/6 mV scale factor determined from atmospheric muon testing. The size of the neutron capture signal is ≈3 pe's in the small boronated scintillator block. Using the calculation method described in section 3.2 with a collection efficiency of 0.6% reflecting the greater fraction of the surface area of scintillator covered by the PMT photocathode here, we find that the number of pe's detected is in very good agreement with the 3.4 pe's expected from a 76 keV energy deposit given in the literature.

Recoils of fast neutrons with protons in the scintillator produce a signal, in the process becoming occasionally thermalized and subsequently being absorbed by the ^{10}B with an expected characteristic time constant of ≈2.7 μs. We timed the interval between consecutive pulses within the boron-loaded and boron-free scintillator blocks. The timing difference distribution should be dominated at large times (beyond fast neutron and gamma-ray accidental coincidences) by this expected ≈2.7 μs time constant. The observed time difference distribution is shown in Fig. 8 for both non-boronated and boronated scintillator blocks. A fit to the boron-loaded distribution indicates a late tail with a time constant of 2.71 μs, as expected. The non-boronated scintillator also exhibits a late tail due to accidental coincidences starting and stopping the clock. The excess signal in the boronated block confirms the presence of the neutron-capture signal.

4.3 CERN Beam Tests

Electron and pion beam tests were conducted at CERN in 2012 for a BSD prototype with the actual flight boronated scintillator equipped with eight R1924 PMTs read out with commercial charge integrating electronics (LeCroy 2249W ADC). The CERN beam test arrangement had the PMTs mounted 12% further apart from each other than in the flight unit. These tests led to the conclusion that the BSD does indeed provide discriminating power between hadrons and electrons, as described below. There was, however, a discrepancy in the observed late signal size compared to expectations from simulations, by a factor of ≈30 (with more light seen than anticipated). The simulation of neutron production, thermalization and capture is tricky and difficult to carry out absolutely. Therefore, two follow up beam tests were conducted in 2015 and 2016 with an identically sized piece of scintillator without any boron (EJ-200), yielding only a scintillation signal without any neutron capture enhancement. These later tests allowed an experimental comparison of the performance of the scintillator with or without boron doping, reducing the dependence on simulations [32]. Note that because of the scheduling requirement to deliver the flight unit for integration into the ISS-CREAM instrument, the boron loaded scintillator slab was not available for any further beam tests beyond 2012. The 2015 and 2016 tests, combined with the results of ground muon tests and UV and non-UV LED tests, indicated that the late signal was dominated by fluorescence emission, with a decay timescale of ≈2 μs. Ground atmospheric muon tests showed that a measurable late fluorescence signal was present on the time scale of 1 - 10 μs. A test with a UV LED (Bivar UV3TZ-395-30, 395 nm peak emission wavelength), which excites the waveshifting fluor of the plastic, also exhibited a late signal, whereas identical tests with a red LED showed no such late signal. Data from the later beam tests were used to fit a three-component model (fast, medium, and slow time scales) of the time dependence of the scintillator light yield. The result is that the fluorescence signal is significant and outweighs the neutron capture signal, but the neutron capture enhancement in the case of the boronated piece does provide discrimination between hadronic and electromagnetic showers. The beam tests and results are described below.

In November 2012 we carried out measurements at the CERN H2 beam line of the response of the BSD exposed to electrons and pions of varying energies (75 GeV to 175 GeV for electrons, 250 to 350 GeV for

pions). For this test the CAL and carbon targets of the ISS-CREAM instrument were also in the beam, upstream of the BSD, so that BSD signals represented realistic flight conditions, with pions serving as hadronic proxies for protons and nuclei. In particular, showers of particles in the CAL could be used to identify similar energy deposits from electron-induced electromagnetic showers and pion-induced hadronic showers. For a comparable CAL signal, pions typically required about 3 times more energy than electrons. For example, Fig. 9 illustrates the measured CAL energy deposit distribution for 125 GeV electrons and 350 GeV pions. A selection is made of events around 2 standard deviations of the electron peak energy deposit. Pions with energy deposits in this region are potential backgrounds against electron identification.

For events selected in Fig. 9 we then study the distribution of signals generated in the BSD, which are a combination of late scintillation light from the shower leaking through the bottom of the CAL plus a contribution from the thermalized neutron echo of the shower. This is shown in Fig. 10 where the total integrated late-light BSD activity is histogrammed in counts of photoelectrons. While these events are selected to have comparable activity in the CAL, they generate different signatures in the BSD, at the bottom of the instrument stack. This is a combination of differences in shower profile between electromagnetic and hadronic events as well as a different neutron harvest between electron and pion (or nucleus) events. GEANT4 simulated signals for the two types of events are also shown and are in good agreement with the measurements. For electron events, the scintillation signal is dominated by the late fluorescence activity since the production of thermal neutrons is limited, but for hadron-induced events the simulations must include the thermalized neutron component to reproduce the measurements (difference between the green and magenta curves). All histograms are normalized to have unit area.

The distributions of Fig. 10 can be selected to retain a certain fraction of the electrons, at the cost of retaining a fraction of the pions which become a background. By progressively cutting harder on the electrons, we retain fewer background pion events. Defining the BSD's rejection power as

$$\text{Rejection power} = \frac{(\text{Fraction of electrons accepted})}{(\text{Fraction of hadrons not rejected})}$$

we show in Fig. 11 the electron/hadron rejection power as a function of electron acceptance efficiency. For example, an electron acceptance efficiency of about 85% leads to a hadron rejection power of about 100. In ISS-CREAM the power of the BSD in separating electron-induced events from backgrounds from protons and nuclei will be combined with pre- and post-calorimeter signals in the TCD and BCD [22] to further refine the identification of the shower profile as having been electromagnetically induced.

In August 2016 the non-boronated slab was exposed to electron and pion beams at the CERN H2 beam line. The beam first passed through $3X_0$ thick lead and $18X_0$ thick iron blocks to initiate and develop showers. A scintillation counter was placed between the lead and iron blocks to identify showers initiating in the first three radiation lengths. In order to understand fully the relative amounts of early and late light generated by the scintillator, in the absence of neutron captures, the scintillator material used was EJ-200, which is the base material to which boron is added to produce EJ-254. Spare flight electronics were available at this test, with a larger dynamic range and smaller minimum charge per count than in the 2012 test. Using a 150 GeV electron beam, the late light integration window times were adjusted to incrementally measure the response as a function of time (Fig. 12). The early (fast) component is the normal scintillation output, and is measured by the trigger tubes, while fluorescence light is measured with the electronics intended to detect neutron captures. A two-component exponential fits the late response, with time scales for the medium and slow components of 490 ns and

2.37 μs, respectively, and a relative integrated yield for medium-to-slow components of 1.08, where the total yield of each component, in number of photons per second, is assumed to be

$$Y_i(t) = \left(\frac{\tau_1+\tau_2}{\tau_2^2}\right)\left(1-e^{-\frac{t}{\tau_1}}\right)\left(e^{-\frac{t}{\tau_2}}\right),$$

properly normalized, with τ_1 = 1.2 ns the rise time for all components and τ_2 the fall time appropriate to the component under consideration. With this model, one can identify the relative total normalized yields for each component to use in the simulations: fast = 95.8%, medium = 2.2%, slow=2.0%. Thus the total yield is

$$Y(t) = N\left(1-e^{-\frac{t}{1.2}}\right)\left[0.142e^{-\frac{t}{7.8}} + 4.4\times10^{-5}e^{-\frac{t}{490}} + 8.4\times10^{-5}e^{-\frac{t}{2370}}\right],$$

where times are in ns, and *N* is an overall normalization to total yield detected. The formula incorporates a rise time for all components of 1.2 ns, and a measured fall time for the fast component of 7.8 ns. Both the rise and fall times are longer than the EJ-200 manufacturer's values of 0.9 ns and 1.2 ns [23], likely due to a folding in of the PMT response. More details of these measurements, including the numerical values in the above equation, appear elsewhere [32]. Note that this model has a result that the ratio of late light to early light is constant, a feature seen in the CERN 2015 data (below).

This response model was applied to data taken in November 2015 at CERN of the response of the scintillator slab exposed to electrons and pions of varying energies (75 GeV to 175 GeV for electrons, 250 to 350 GeV for pions), again using the non-boronated EJ-200 piece of scintillator. The rest of the ISS-CREAM instrument was also in the beam, upstream of the scintillator, so that signals represented realistic flight conditions. Once again, showers of particles in the CAL could be used to identify similar energy deposits from electron-induced electromagnetic showers and pion-induced hadronic showers. For example, Fig. 13 shows the measured CAL energy deposit distribution for 125 GeV electrons and 350 GeV pions. A selection is made of events around the range of the electron peak energy deposit. Hadrons (pions) in this region are potential backgrounds against electron identification.

For events selected in Fig. 13, with the additional requirement that the shower start by the third layer (3 X_0) of the CAL, we then study the distribution of signals generated in the non-boronated BSD proxy, which are from the late scintillation light from the shower leaking through the bottom of the CAL. In flight, this signal also includes an additional contribution from the thermalized neutron echo of the shower. The total integrated late signal consists of the sum of seven PMT signals, each normalized to the response of beam muons created when a steel beam stop was inserted upstream of the detector. The measured distributions are shown in Fig. 14. While these events are selected to have comparable activity in the CAL, they generate different signatures in the BSD at the bottom of the instrument stack. This is due to differences in shower profile between electromagnetic and hadronic events. GEANT4 simulated signals for the two types of events are also shown using the late fluorescence contributions only, as no thermal neutrons contribute to the non-boronated scintillator output; the simulated distributions are in good agreement with the measurements.

The fluorescence and neutron capture signal models are both normalized to the measured collection efficiency of muons through the center of the detector, as discussed in Section 2. In the simulation, scintillation photons are counted at production. Neutron captures occurring within the late time window are counted using ^{7}Li production as a proxy for the process, and 570 photons/capture are added. Both photon counts are smeared with Poisson statistics. The simulations indicate that the relative signal due to neutron captures is most often (52% of the time) 0 for 125 GeV electrons, for a net mean value of 6.5%, and otherwise has a population with a peak at 8%. For 350 GeV pions, the signal peaks at 15% and has a mean of 23%. This is shown in Fig. 15.

The distributions of Figs. 13 and 14 are compared to the results of simulations using the GEANT4 particle physics package, with the updated scintillation model of Fig. 12, which includes the late fluorescence component. Distributions are generally well matched for both the CAL and BSD-proxy early and late light. An attempt is made to repeat the analysis of Fig. 11 to try and determine a hadron rejection power resulting from the use of the non-boronated scintillator slab in the CERN 2015 beam test. Thus here only the scintillation light is available, without the benefit of the neutron capture signal. The result is shown in Fig. 16, in comparison with the distribution for the boronated scintillator. Without boron loading and thus no sensitivity to thermal neutrons, a much more modest rejection power is achieved: at 80% electron acceptance efficiency, a rejection power of about 15 is achieved, compared to about 100 when neutron capture enhancements to the BSD signals are present. The differences between the measured hadron rejection power with or without boron doping are striking. In ISS-CREAM the power of the BSD in separating electron-induced events from backgrounds from protons and nuclei is combined with pre- and post-calorimeter signals in the TCD and BCD to further refine the identification of the shower profile as having been electromagnetically induced. This analysis is in progress, but the importance of the BSD discrimination lies in the independence of this discrimination from the shower shape determined by the CAL and TCD/BCD.

5. Deployment and Flight Operations

The boronated scintillator detector was delivered to NASA's Wallops Flight Facility in July 2014. Prior to this, its electronics underwent thermal/vacuum testing at NASA's Goddard Space Flight Facility and the assembled enclosures went through a vibration test at Washington Laboratories in Frederick, Maryland, to ensure they would survive launch. The detector was integrated into the ISS-CREAM instrument and passed all instrument-level tests with only minor issues that were easily addressed.

The ISS-CREAM payload was delivered to Kennedy Space Center in August 2015 and launched on the SpaceX CRS-12 mission to the ISS in August of 2017. Continuous data taking operations began August 22, 2017, with interruptions at first for ISS transits of the South Atlantic anomaly, when the instrument was adjusted to a quiescent, low-power state to protect it from radiation damage owing to the enhanced low-energy radiation impacting it; this practice was discontinued in September 2018, transitioning to fully powered operations at all times, for a significantly improved duty cycle. The performance studies of the BSD described here and the Monte Carlo simulations developed to describe its response were brought to bear in adjusting its operational gains in flight so as to ensure a dynamic range response suited for the detection and reconstruction of electron-induced events up to 10 TeV. The BSD operated stably and in flight science mode starting early October, 2017. The performance in flight of the BSD and science results deriving from it will be the subject of forthcoming publications.

6. Conclusions

The use of a boronated scintillator detector in the ISS-CREAM detector provides sensitivity to the tail of cosmic-ray induced showers leaking out of the bottom of the calorimeter. It also provides a measure of the yield of thermalized neutrons produced in the particle interactions in the instrument. The neutron harvest is sensitive to the nature of the incident particle, with nuclei producing them more copiously than an incident cosmic-ray electron, and thus the BSD is part of the strategy (together with the shower shape) to identify electrons and measure their spectrum into the multi-TeV regime, where it is poorly known. The neutron echo of the particle cascade through the ISS-CREAM instrument is integrated at late times, from 900 ns through 4.9 μs after the primary particle incidence. This late time regime is

potentially affected by a significant amount of late fluorescence and/or afterpulsing, if the incident shower activity in the scintillator is large enough, and thus a dynode-gating scheme was implemented to activate the majority of the BSD PMTs (that were otherwise insensitive to the initial light flash) to carry out the signal integration into the multi-μs regime. The design of the BSD and its response characterization with laboratory tests using a radioactive neutron source, or cosmic-ray muons, and with electron and pion beams at CERN, were presented here, and electron/hadron discrimination from the thermal neutron yield differences was demonstrated.

The measurements at CERN, combined with the other measurements presented here, have led us to understand and characterize a slow component of the scintillator yield that is significantly brighter than the neutron capture signal. The existence of late fluorescence with microsecond timescales is of potential interest to particle detector designs using scintillator in high rate environments, such as accelerators, but especially to applications where signal measurements extend into the multi-microsecond region, such as some cryogenic dark matter detectors [38].

Acknowledgements

The authors thank NASA GSFC and WFF for project management and engineering support, and NASA JSC ISS Program Office for launch support and the ISS accommodation. This work was supported in the U.S. by NASA grants NNX17AB43G, NNX17AB42G, NNX17AB41G and their predecessor grants, as well as by directed RTOP funds to NASA GSFC WFF. It was supported in Korea by the Creative Research Initiatives of MEST/NRF, and by Basic Science Research Program through the National Research Foundation of Korea (NRF) funded by the Ministry of Education (2016R1D1A1B03934341). It was supported in France by IN2P3/CNRS and CNES and in Mexico by DGAPA-UNAM and CONACYT. The authors also thank M. Geske, Penn State, for contributions to the BSD, K. Wallace at Northern Kentucky University for contributions to Monte Carlo simulations and the CERN beam test, M. McGinnis, J. Cantwell and E. Cofie at SGT for work on the mechanical design, and to CERN personnel for support during beam tests, in particular A. Fabich and M. Jeckel. We would also like to thank C. Hurlbut and C. Maxwell at Eljen Technologies for providing information on the characteristics of the doped and undoped scintillators as well as small samples for development and testing.

References

[1] Y. Amare, et al., ISS-CREAM Collaboration, “The Cosmic Ray Energetics And Mass Instrument on the International Space Station (ISS-CREAM),” in preparation, to be submitted to JINST (2019)

[2] H.S. Ahn, et al., CREAM Collaboration, “Discrepant hardening observed in cosmic-ray elemental spectra,” Astrophys. J. 714 (2010) L84

[3] O. Adriani, et al., PAMELA Collaboration, “PAMELA measurements of cosmic-ray proton and helium spectra,” Science 332 (2011) 69

[4] M. Aguilar, et al., AMS Collaboration, “Properties of elementary particle fluxes in primary cosmic rays measured with the Alpha Magnetic Spectrometer on the ISS,“ Proc. of the 35th Int. Cosmic Ray Conf., Busan, South Korea (2017)

[5] R.D. Blandford and J.P. Ostriker, “Particle acceleration by astrophysical shocks,” ApJ 221, L29 (1978)

[6] D. Caprioli, “Cosmic-ray acceleration in supernova remnants: non-linear theory revised,” JCAP 07, 038 (2012)

[7] A.M. Hillas, “Can diffusive shock acceleration in supernova remnants account for high-energy galactic cosmic rays? ,” J. Phys. G: Nucl. Part. Phys. 31, R95 (2005)

[8] V. Ptuskin, V. Zirakashvili and E.S. Seo, “Spectra of cosmic-ray protons and helium produced in supernova remnants,” ApJ 763, 47 (2013)

[9] S. Thoudam and J. Hörandel, “Revisiting the hardening of the cosmic ray energy spectrum at TeV energies,” MNRAS 435, 2532 (2013)

[10] R. Aloisio, P. Blasi and P.D. Serpico, “Nonlinear cosmic ray Galactic transport in the light of AMS-02 and Voyager data,” A&A 583, A95 (2015)

[11] Y.S. Yoon, et al., CREAM Collaboration, “Proton and helium spectra from the CREAM-III flight,” Astrophys. J. 839 (2017) 5

[12] T.K. Gaisser, T. Stanev and S. Tilav, “Cosmic ray energy spectrum from measurements of air showers,” Frontiers of Physics 8, 748 (2013)

[13] I.A. Grenier, J.H. Black, and A.W. Strong, “The Nine Lives of Cosmic Rays in Galaxies,” Annu. Rev. Astron. Astrophys. 53, 199 (2015)

[14] S.C.C. Ting, et al., AMS-02 Collaboration, “The Alpha Magnetic Spectrometer on the International Space Station,” Nucl. Phys. B (Proc. Suppl.) 243 (2013) 12

[15] E. Atkin, et al., NUCLEON Collaboration, “The NUCLEON space experiment for direct high energy cosmic rays investigation in TeV–PeV energy range,” Nucl. Inst. & Meth. A 770 (2015) 189

[16] S. Torii, et al., CALET Collaboration, “The CALorimetric Electron Telescope (CALET): High Energy Astroparticle Physics Observatory on the International Space Station,” Proc. of the 34th Int. Cosmic Ray Conf., The Hague, The Netherlands, PoS(ICRC2015)581 (2015)

[17] J. Chang, et al., DAMPE Collaboration, “The DArk Matter Particle Explorer mission,” Astropart. Phys. 95 (2017) 6

[18] H.S. Ahn, et al., CREAM Collaboration, “The Cosmic Ray Energetics and Mass (CREAM) instrument,” Nucl. Inst. and Meth. A 579 (2007) 1034

[19] J. Lee, et al., ISS-CREAM Collaboration, “Design, fabrication and performance of the silicon charge detector for the ISS-CREAM” Proc. of the 34th Int. Cosmic Ray Conf., The Hague, The Netherlands, PoS(ICRC2015)693 (2015)

[20] H.J. Hyun, et al., ISS-CREAM Collaboration, “Performances of photodiode detectors for top and bottom counting detectors of ISS-CREAM experiment,” Nucl. Inst. and Meth. A 787 (2015) 134

[21] Y. Amare, et al., ISS-CREAM Collaboration, “Performance of the ISS-CREAM calorimeter: results of beam tests,” in preparation, to be submitted to Nucl. Inst. and Meth. A (2019)

[22] Y.S. Hwang, et al., ISS-CREAM Collaboration, “Construction and Testing of a Top Counting Detector and a Bottom Counting Detector for the Cosmic Ray Energetics And Mass Experiment on the International Space Station,” JINST 10 (07), P07018 (2015)

[23] EJ-200 and EJ-254 plastic data sheets. Eljen Technologies http://eljentechnology.com

[24] D.M. Drake, W.C. Feldman, and C. Hurlbut, “New Electronically Black Neutron Detectors,” Nucl. Inst. and Meth. A 247 (1986) 576

[25] C. Hurlbut, Eljen Technology, private communication (2017)

[26] M. Sampson, "Tin Whiskers: Amendment", NASA Parts Advisory NA-044A, December 17, 1998

[27] “Space Station Ionizing Radiation Design Environment,” NASA document SSP 30512 Revision C (1994)

[28] T.B. Anderson, “Exploring the Cosmic Ray Spectrum with the CREAM Experiment”, Ph.D. Thesis, Penn State University (2013) https://inspirehep.net/record/1418241/files/Thesis-2013-Anderson.pdf

[29] S. Agostinelli, et al., "Geant4 - a simulation toolkit," Nucl. Inst. and Meth. A 506 (2003) 250

[30] T.B. Anderson, et al., ISS-CREAM Collaboration, “The ISS-CREAM Boronated Scintillator Detector,” Proc. of the 33rd Int. Cosmic Ray Conf., Rio de Janeiro, Brazil (2013)

[31] J.G. Pronko and J.L. Guttman, “Absolute Fluorescence Yields of Long and Short Term Decay Components of Selected Scintillators,” Nucl. Inst. and Meth. A 332 (1993) 121

[32] S. Nutter et al., “Measurement of light yield of particle scintillation in plastic scintillator from one to ten microseconds,” submitted to Nucl. Inst. and Meth. A (2019)

[33] “Hamamatsu R1924A Photomultiplier Tube Datasheet,” https://www.hamamatsu.com/resources/pdf/etd/R1924A_TPMH1280E.pdf

[34] J.T. Link, et al., Super-TIGER Collaboration, “Scintillation Detector for the Measurement of Ultra-Heavy Cosmic Rays on the Super-TIGER Experiment”, Proc. of the 32nd Int. Cosmic Ray Conf., Beijing, China (2011)

[35] G.J. Hurford and D.W. Curtis (2003) “The PMTRAS Roll Aspect System on RHESSI,” in: R.P. Lin, B.R. Dennis and A.O. Benz (eds), “The Reuven Ramaty High-Energy Solar Spectroscopic Imager (RHESSI),” Springer, Dordrecht (2003)

[36] F.D. Martini and K.P. Wacks, “Photomultiplier Gate for Stimulated-Spontaneous Light Scattering Discrimination,” Rev. of Sci. Inst. 38 (1967) 886

[37] T.B. Anderson, et al., ISS-CREAM Collaboration, “Photomultiplier Dynode Gating Scheme for the Boronated Scintillator Detector of the ISS-CREAM Experiment,” submitted to Nucl. Inst. and Meth. A (2019)

[38] E. Segreto, “Evidence of delayed light emission of tetraphenyl-butadiene excited by liquid-argon scintillation light,” Phys. Rev. C 91, 035503 (2015)

Fig. 1. ISS-CREAM instrument, with exploded schematic view (left) and photo of final integrated instrument (right). Identified from top to bottom are the silicon charge detector, carbon targets, top counting detector, calorimeter, bottom counting detector and boronated scintillator detector, respectively.

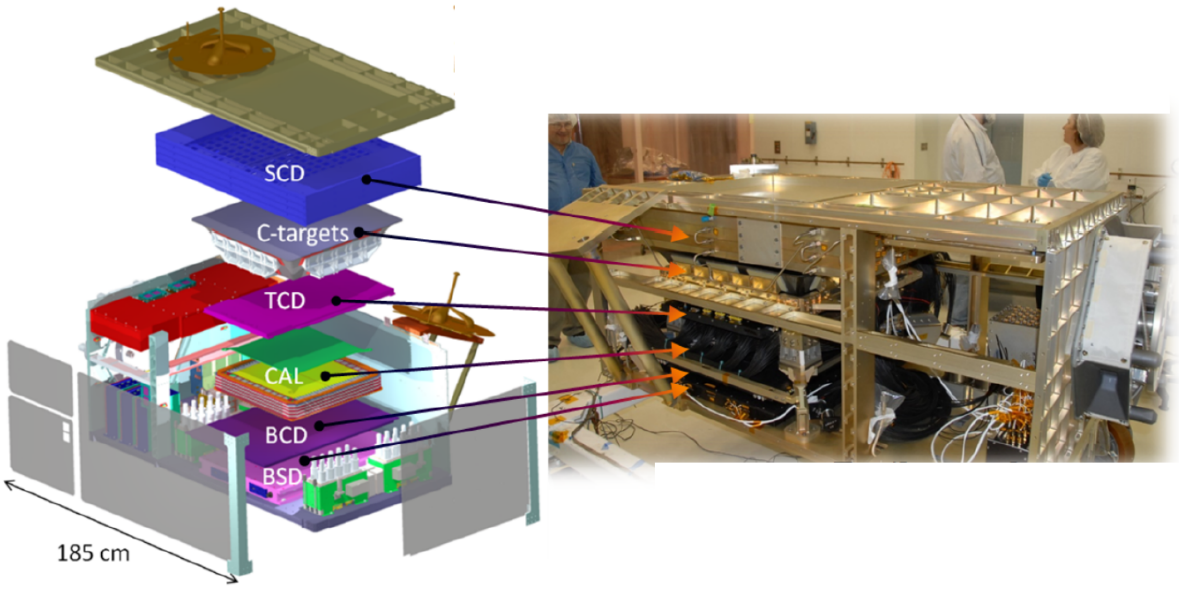

Fig. 2. BSD detector enclosure (black crate with white coiled cables) mounted on the pallet at the bottom of the ISS-CREAM instrument stack. Also visible at the top-left is the black BSD electronics enclosure.

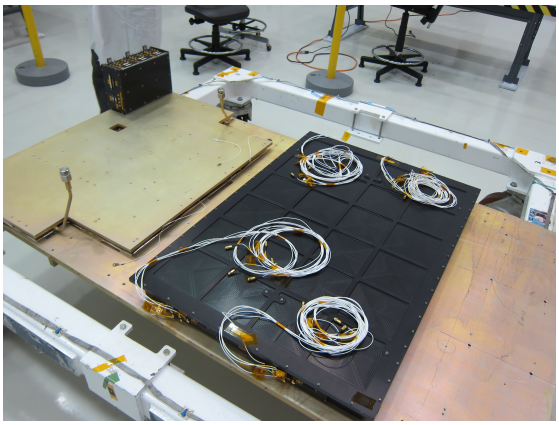

Fig. 3. Schematic representation of the BSD electronics (left) and detector (right) enclosures. The representation is not to scale.

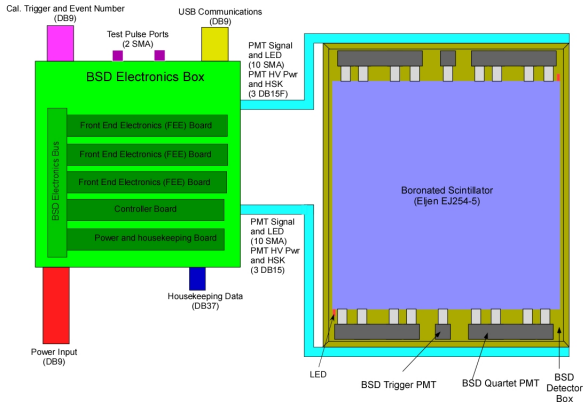

Fig. 4. Mechanical drawing of the BSD detector enclosure (left). One corner of the BSD detector box (right) depicts a quartet PMT assembly unit and a trigger PMT assembly.

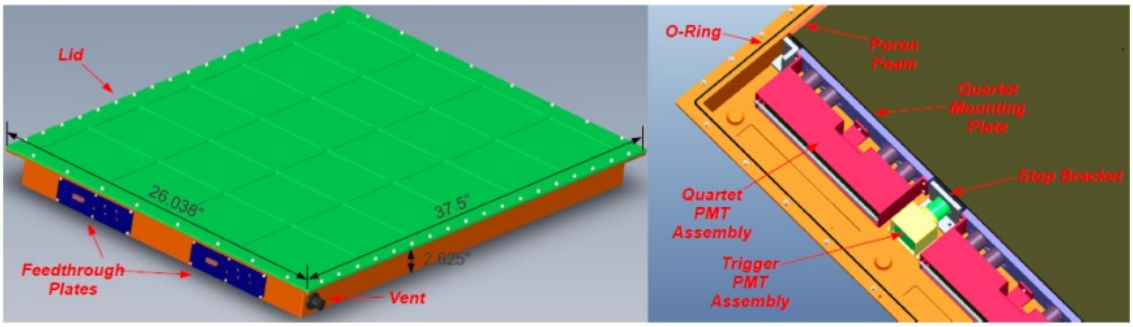

Fig. 5. Timing diagram of the BSD readout electronics illustrating the two trigger PMT signals from the prompt shower event, the initiation of the DON signal to ramp up the quartet PMT dynodes, the switching transient resulting from the dynodes powering on, and the integration window for the late light activity in the boronated scintillator.

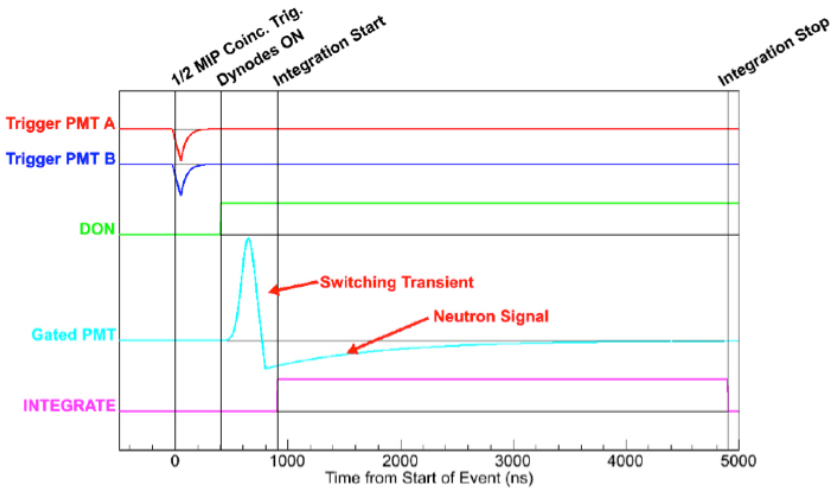

Fig. 6. Setup used for ^{252}Cf tests. The boron-free (non BSD) and boron-loaded (BSD) scintillator blocks are exposed to gamma rays, fast and slow neutrons from a 4.23 mrem/hr source. A lead absorber sheet reduces the gamma-ray background, and polyethylene boards increase the thermal neutron signal. Distances indicated are not to scale.

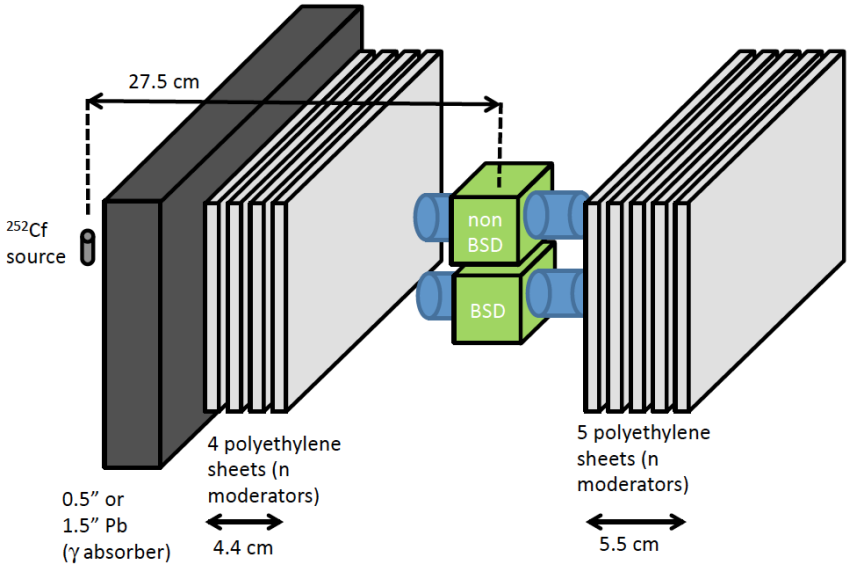

Fig. 7. Integral count rates in the boron-loaded scintillator (BSD, circles) and the boron-free scintillator (non BSD, inverted triangles), as a function of trigger threshold voltage. The rates are measured with a 0.5” (left) or 1.5” (right) thickness of lead between the ^{252}Cf source and the scintillator blocks. The reduced rates with thicker lead are attributable to the absorption of the gamma rays from the source. The excess signal of the BSD block over the non-BSD block is attributable to the neutron capture signal. Statistical uncertainties are smaller than the symbol sizes.

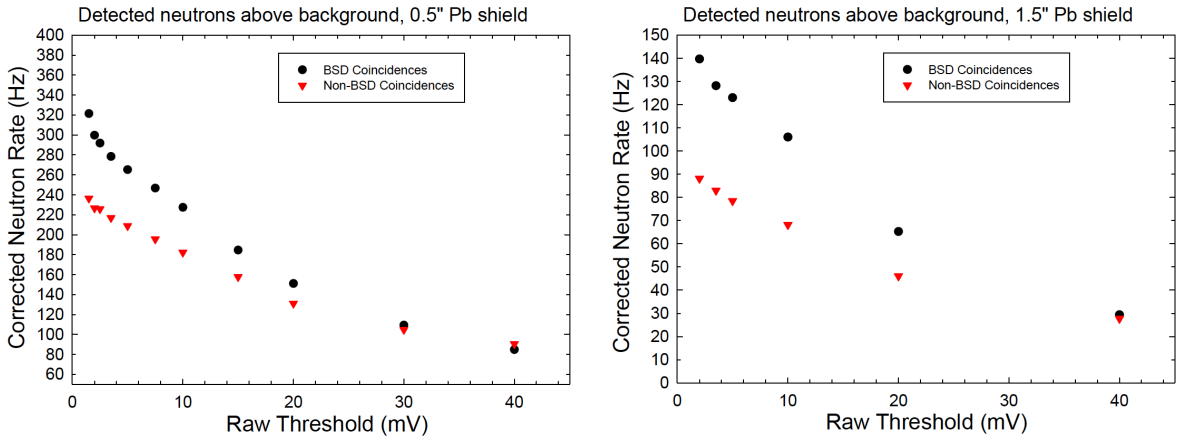

Fig. 8. Distribution of time differences between consecutive signals in the boron-loaded (black points) and boron-free (gray points) scintillators exposed to the ^{252}Cf source. The fit to the late tail of the boron-loaded distribution, indicated by a solid gray line, has an exponential time constant of 2.71 µs.

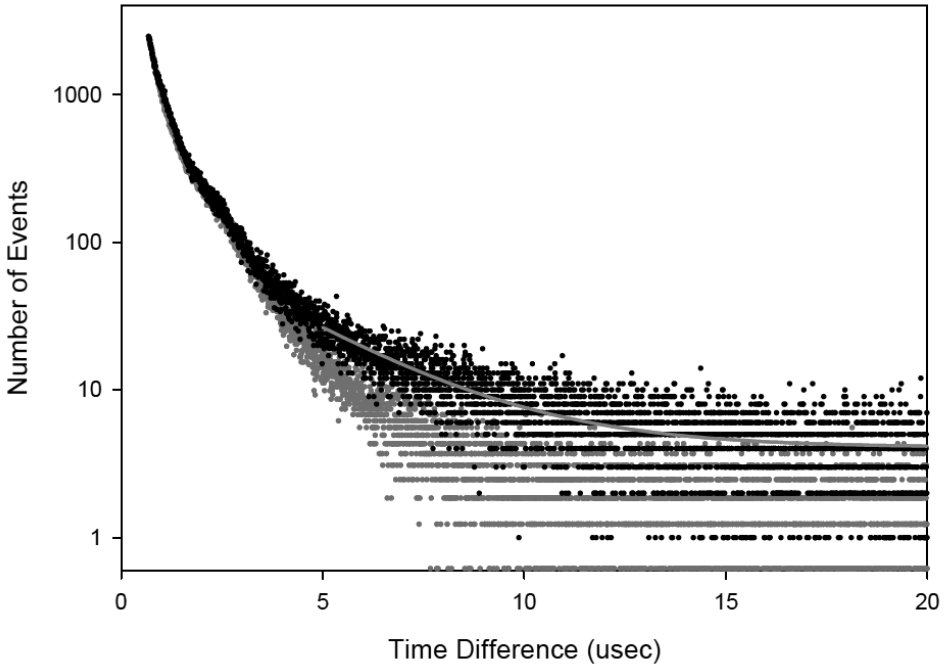

Fig. 9. Distribution of total integrated energy deposited in the CAL,in the CERN 2012 beam test by 125 GeV electrons (solid histogram) and 350 GeV pions (dotted histogram). The calorimeter signal tallies the energy deposited in the 5 contiguous ribbons of any given layer, with the center ribbon being the one with largest activity. The event selection identified by the vertical black lines represents two standard deviations of the electron peak (fitted to a Gaussian). Hadronic showers in this different energy range from electromagnetic showers are potential backgrounds to any cosmic-ray electron measurement.

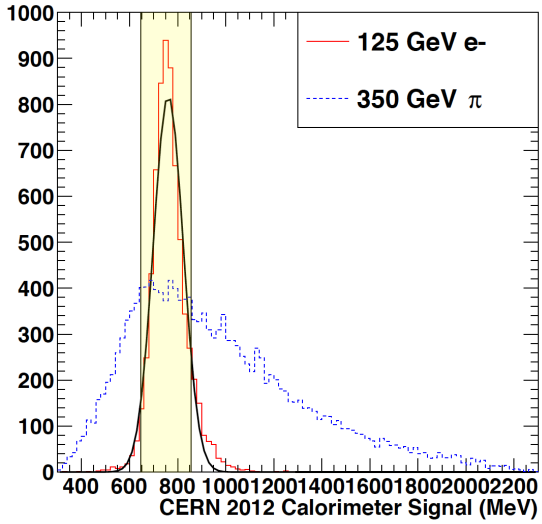

Fig. 10. For the event selection of Fig. 9, the integrated late activity in the BSD (in photoelectrons) is shown for the 125 GeV electrons and the 350 GeV pions (same graph with linear (left) and logarithmic (right) scales). Measurements are the solid left (electrons) and solid right (pions) histograms, and are compared with GEANT4-based simulations in short dash lines using the fluorescence model described in the text. The long dash histograms are the results of the fluorescence model augmented by light from neutron captures, which only affects the hadron-induced events.

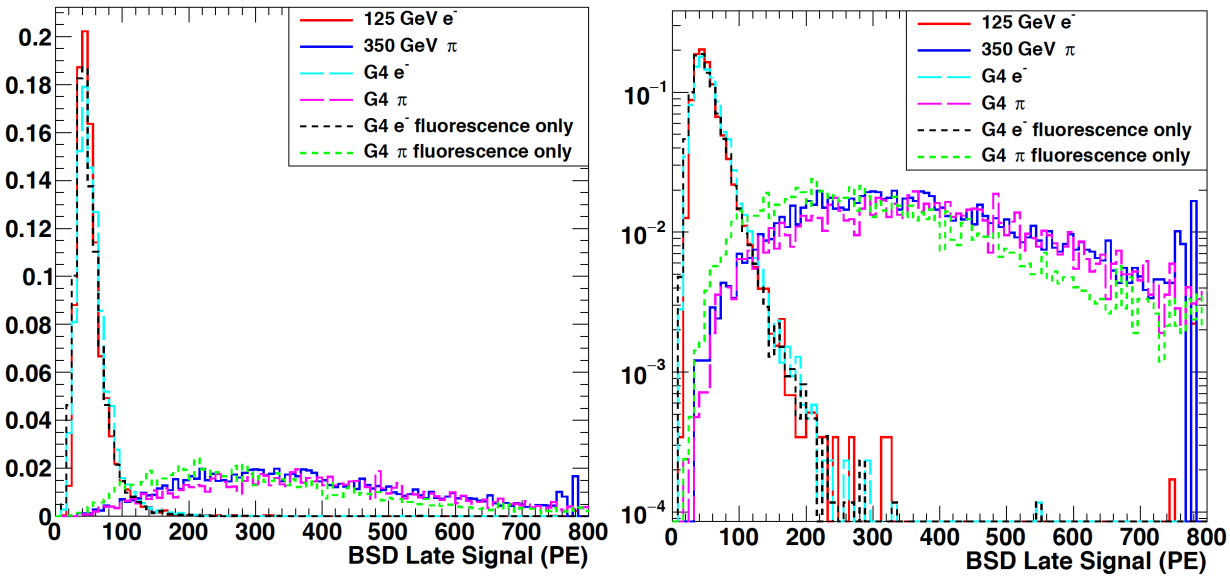

Fig. 11. Measured and simulated electron/hadron rejection power as a function of electron acceptance efficiency for the CERN 2012 data with the actual boron-loaded scintillator flown with the ISS-CREAM instrument. Error bars are statistical. The lines connecting the points are merely guides to the eye, and the apparent disagreement between data and Monte Carlo at an electron detection efficiency less than 0.9 is not statistically significant.

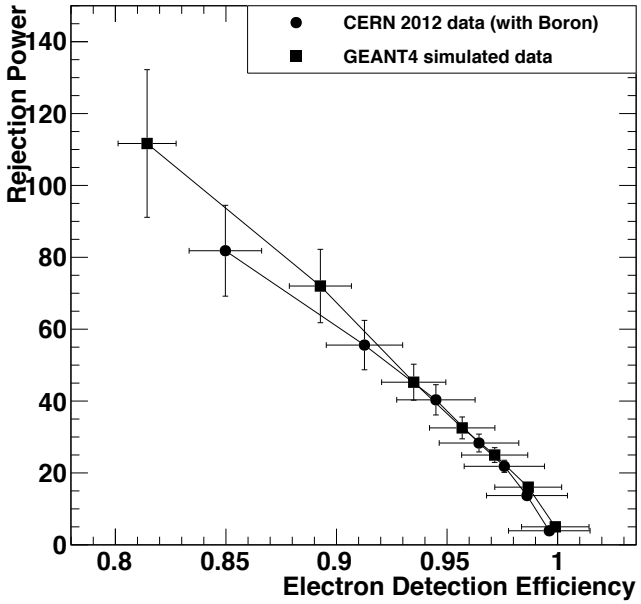

Fig. 12. The signal measured during the 2016 CERN beam test for late (slow fluorescence) light generated in the EJ-200, non-boronated scintillator from 1 to 10 μs after the beam particle shower passed through the detector. Error bars are statistical. A two component exponential fits the data [32].

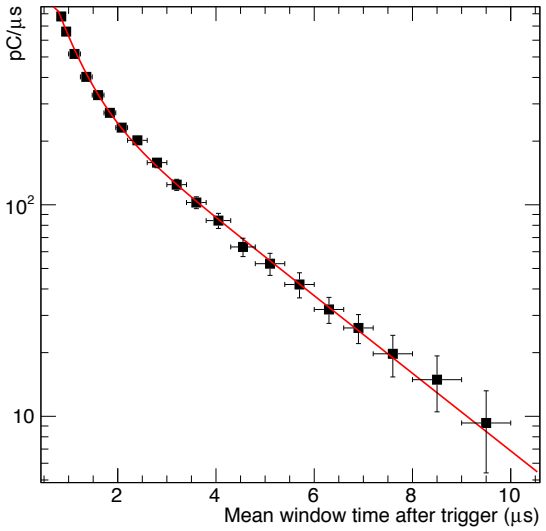

Fig. 13. Histogram of the relative number of events with total integrated energy deposited in the CAL in the 2015 beam test for 125 GeV electrons (high solid histogram) and 350 GeV pions (low solid histogram). The event selection identified by the shaded region is used in this analysis. Distributions from GEANT4 simulated events of the same number of incident particles of each energy and type are also shown as dashed lines.

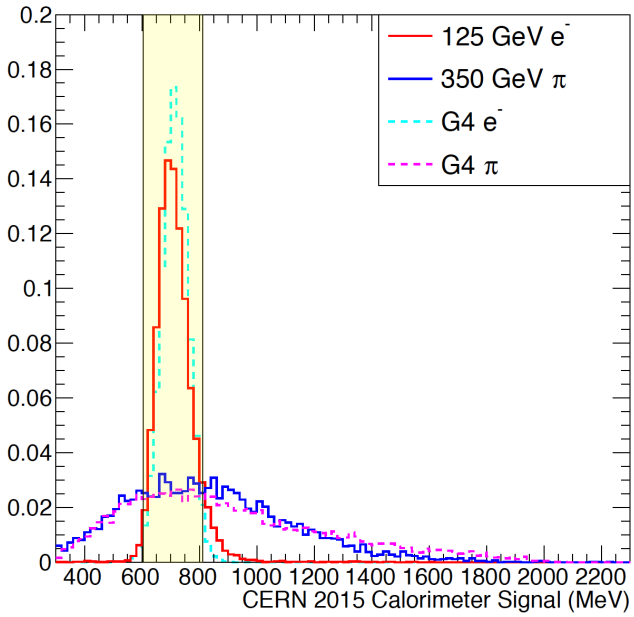

Fig. 14. For the event selection of Fig. 13, the integrated late activity (in photoelectrons) in the non-boronated BSD proxy is shown for the electrons and pions for the data and GEANT4 simulations which use the late fluorescence model presented (no thermal neutrons are included here). The same line scheme is used as in the previous figure.

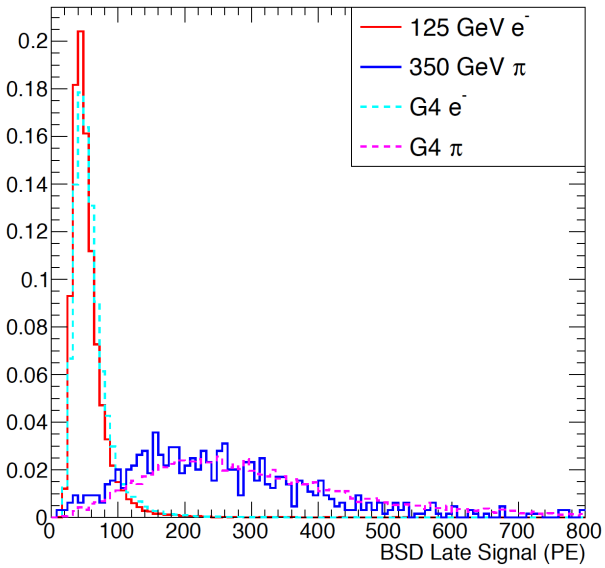

Fig. 15. Relative photon production due to neutron captures and late fluorescence in the simulation model. Fluorescence photons and neutron captures are counted during the simulation, then Poisson smeared and normalized to the measured muon signal collection efficiency. See text for details. Distributions are normalized to have unit area, and the large population of zero capture events (≈52%) in the electron distribution is truncated. This histogram illustrates the method behind the BSD hadron rejection: hadron- and electron-initiated events which deposit the same energy in the calorimeter have different neutron components in the showers.

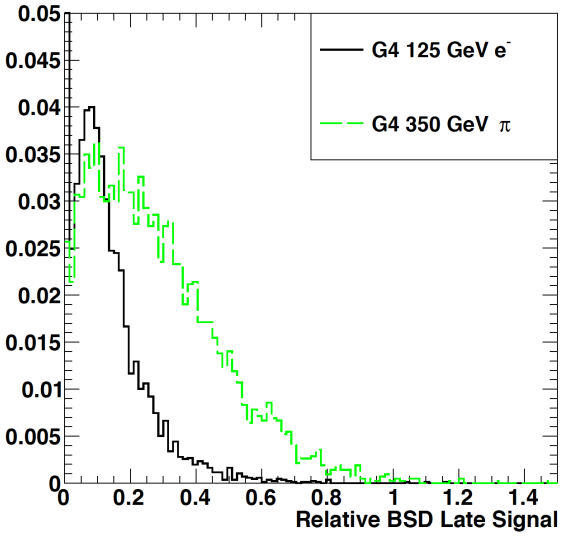

Fig. 16. Electron/hadron rejection power shown as a function of electron acceptance efficiency for the boronated scintillator detector (filled squares, from Fig. 11) compared with a similar measure for the non-boronated scintillator detector (filled circles). The presence of slow neutron captures in the case of the boronated detector enables the identification of electron events.